Plasmon modes in single gold nanodiscs

K. Imura,[1,*] K. Ueno,[2] H. Misawa,[2] H. Okamoto,[3] D. McArthur,[4] B. Hourahine,[4] and F. Papoff[4]

[1]*Department of Chemistry and Biochemistry, School of Science and Engineering, Waseda University, Okubo, Shinjuku, Tokyo 169-8555, Japan*
[2]*Research Institute for Electronic Science, Hokkaido University, Kita-Ku, Sapporo, Hokkaido 001-0021, Japan*
[3]*Institute for Molecular Science and The Graduate University for Advanced Studies, Myodaiji, Okazaki 444-8585, Japan*
[4]*SUPA, Department of Physics, University of Strathclyde, 107 Rottenrow, Glasgow G4 0NG, UK*
[*]*imura@waseda.jp*

Abstract: Optical properties of single gold nanodiscs were studied by scanning near-field optical microscopy. Near-field transmission spectra of a single nanodisc exhibited multiple plasmon resonances in the visible to near-infrared region. Near-field transmission images observed at these resonance wavelengths show wavy spatial features depending on the wavelength of observation. To clarify physical pictures of the images, theoretical simulations based on spatial correlation between electromagnetic fundamental modes inside and outside of the disc were performed. Simulated images reproduced the observed spatial structures excited in the disc. Mode-analysis of the simulated images indicates that the spatial features observed in the transmission images originate mainly from a few fundamental plasmon modes of the disc.

OCIS codes: (180.0180) Microscopy; (160.4236) Nanomaterials; (180.4243) Near-field microscopy; (240.6680) Surface plasmons; (290.5850) Scattering, particles.

References and links

1. M. E. Stewart, C. R. Anderton, L. B. Thompson, J. Maria, S. K. Gray, J. A. Rogers, and R. G. Nuzzo, "Nanostructured plasmonic sensors," Chem. Rev. **108**(2), 494–521 (2008).
2. C. Valsecchi and A. G. Brolo, "Periodic metallic nanostructures as plasmonic chemical sensors," Langmuir **29**(19), 5638–5649 (2013).
3. P. Anger, P. Bharadwaj, and L. Novotny, "Enhancement and quenching of single-molecule fluorescence," Phys. Rev. Lett. **96**(11), 113002 (2006).
4. S. Kühn, U. Håkanson, L. Rogobete, and V. Sandoghdar, "Enhancement of single-molecule fluorescence using a gold nanoparticle as an optical nanoantenna," Phys. Rev. Lett. **97**(1), 017402 (2006).
5. G. C. Schatz and R. P. Van Duyne, "Electromagnetic mechanism of surface-enhanced spectroscopy, " in *Handbook of Vibrational Spectroscopy*, J. M. Chalmers and P. R. Griffiths, eds. (Wiley, 2002).
6. M. Moskovits, "Surface-enhanced Raman spectroscopy: a brief retrospective," J. Raman Spectrosc. **36**(6–7), 485–496 (2005).
7. W. L. Barnes, A. Dereux, and T. W. Ebbesen, "Surface plasmon subwavelength optics," Nature **424**(6950), 824–830 (2003).
8. M. A. Noginov, G. Zhu, A. M. Belgrave, R. Bakker, V. M. Shalaev, E. E. Narimanov, S. Stout, E. Herz, T. Suteewong, and U. Wiesner, "Demonstration of a spaser-based nanolaser," Nature **460**(7259), 1110–1112 (2009).
9. M. W. Knight, H. Sobhani, P. Nordlander, and N. J. Halas, "Photodetection with active optical antennas," Science **332**(6030), 702–704 (2011).
10. U. Kreibig and M. Vollmer, *Optical Properties of Metal Clusters* (Springer, 1995).
11. K. L. Kelly, E. Coronado, L. L. Zhao, and G. C. Schatz, "The optical properties of metal nanoparticles: The influence of size, shape, and dielectric environment," J. Phys. Chem. B **107**(3), 668–677 (2003).
12. C. F. Bohren and D. R. Huffman, *Absorption and Scattering of Light by Small Particles* (Wiley, 1983).
13. K. Imura, T. Nagahara, and H. Okamoto, "Near-field optical imaging of plasmon modes in gold nanorods," J. Chem. Phys. **122**(15), 154701 (2005).
14. D. Rossouw, M. Couillard, J. Vickery, E. Kumacheva, and G. A. Botton, "Multipolar plasmonic resonances in silver nanowire antennas imaged with a subnanometer electron probe," Nano Lett. **11**(4), 1499–1504 (2011).

#206576 - $15.00 USD Received 26 Feb 2014; revised 25 Apr 2014; accepted 29 Apr 2014; published 13 May 2014

15. B. S. Guiton, V. Iberi, S. Li, D. N. Leonard, C. M. Parish, P. G. Kotula, M. Varela, G. C. Schatz, S. J. Pennycook, and J. P. Camden, "Correlated optical measurements and plasmon mapping of silver nanorods," Nano Lett. **11**(8), 3482–3488 (2011).
16. I. Alber, W. Sigle, S. Müller, R. Neumann, O. Picht, M. Rauber, P. A. van Aken, and M. E. Toimil-Molares, "Visualization of multipolar longitudinal and transversal surface plasmon modes in nanowire dimers," ACS Nano **5**(12), 9845–9853 (2011).
17. C. Sönnichsen, T. Franzl, T. Wilk, G. von Plessen, J. Feldmann, O. Wilson, and P. Mulvaney, "Drastic reduction of plasmon damping in gold nanorods," Phys. Rev. Lett. **88**(7), 077402 (2002).
18. P. Hanarp, M. Käll, and D. S. Sutherland, "Optical properties of short range ordered arrays of nanometer gold disks prepared by colloidal lithography," J. Phys. Chem. B **107**(24), 5768–5772 (2003).
19. C. Langhammer, B. Kasemo, and I. Zorić, "Absorption and scattering of light by Pt, Pd, Ag, and Au nanodisks: Absolute cross sections and branching ratios," J. Chem. Phys. **126**(19), 194702 (2007).
20. A. Taflove and S. C. Hagness, *Computational Electrodynamics: The Finite-Difference Time-Domain Method*, 3rd ed. (Artech House, 2005).
21. B. T. Draine and P. J. Flatau, "Discrete-dipole approximation for scattering calculations," J. Opt. Soc. Am. A **11**(4), 1491–1499 (1994).
22. F. Papoff and B. Hourahine, "Geometrical Mie theory for resonances in nanoparticles of any shape," Opt. Express **19**(22), 21432–21444 (2011).
23. K. Holms, B. Hourahine, and F. Papoff, "Calculation of internal and scattered fields of axisymmetric nanoparticles at any point in space," J. Opt. A, Pure Appl. Opt. **11**(5), 054009 (2009).
24. B. Hourahine, K. Holms, and F. Papoff, "Accurate light scattering for non spherical particles from Mie-type theory," J. Phys. Conf. Ser. **367**, 012010 (2012).
25. B. Hourahine and F. Papoff, "The geometrical nature of optical resonances: from a sphere to fused dimer nanoparticles," Meas. Sci. Technol. **23**(8), 084002 (2012).
26. D. McArthur, B. Hourahine, and F. Papoff, "Evaluation of E.M. fields and energy transport in metallic nanoparticles with near field excitation," Phys. Sci. Int. J. **4**, 565–575 (2014).
27. K. Ueno, S. Juodkazis, V. Mizeikis, K. Sasaki, and H. Misawa, "Spectrally-resolved atomic-scale length variations of gold nanorods," J. Am. Chem. Soc. **128**(44), 14226–14227 (2006).
28. H. Okamoto and K. Imura, "Visualizing the optical field structures in metal nanostructures," J. Phys. Chem. Lett. **4**(13), 2230–2241 (2013).
29. K. Imura, K. Ueno, H. Misawa, and H. Okamoto, "Anomalous light transmission from plasmonic-capped nanoapertures," Nano Lett. **11**(3), 960–965 (2011).
30. K. Imura, T. Nagahara, and H. Okamoto, "Characteristic near-field spectra of single gold nanoparticles," Chem. Phys. Lett. **400**(4–6), 500–505 (2004).
31. K. Imura, T. Nagahara, and H. Okamoto, "Near-field two-photon-induced photoluminescence from single gold nanorods and imaging of plasmon modes," J. Phys. Chem. B **109**(27), 13214–13220 (2005).
32. J. A. Veerman, M. F. Garcia-Parajo, L. Kuipers, and N. F. van Hulst, "Single molecule mapping of the optical field distribution of probes for near-field microscopy," J. Microsc. **194**(2–3), 477–482 (1999).
33. F. P. Schmidt, H. Ditlbacher, U. Hohenester, A. Hohenau, F. Hofer, and J. R. Krenn, "Dark plasmonic breathing modes in silver nanodisks," Nano Lett. **12**(11), 5780–5783 (2012).
34. A. Drezet, M. J. Nasse, S. Huant, and J. C. Woehl, "The optical near-field of an aperture tip," Europhys. Lett. **66**(1), 41–47 (2004).
35. E. A. Coronado and G. C. Schatz, "Surface plasmon broadening for arbitrary shape nanoparticles: A geometrical probability approach," J. Chem. Phys. **119**(7), 3926–3934 (2003).
36. M. Paulus, P. Gay-Balmaz, and O. J. F. Martin, "Accurate and efficient computation of the Green's tensor for stratified media," Phys. Rev. E Stat. Phys. Plasmas Fluids Relat. Interdiscip. Topics **62**(4), 5797–5807 (2000).

1. Introduction

Plasmonics has become an important research field in optics and materials science, with various applications that utilize the unique optical characteristics of plasmonic materials, such as chemical sensors [1,2], surface enhanced spectroscopies [3–6], nano-optical devices [7–9], and so forth. The investigation of spectral and spatial features of plasmons is important both for understanding the basic physical properties of plasmonic materials and to develop practical and useful applications of plasmons. The spectral properties of plasmonic materials have been widely investigated [10–12]. It has been well established that optical properties of single nanoparticles, whose spatial scales are sufficiently smaller than that of wavelength of the interacting light, are explained by the dipolar approximation. The dependence of the optical properties of nanoparticles on size and shape can be also explained by introducing the depolarization factor [12]. In large nanoparticles, on the other hand, the contribution of multipolar plasmon resonances becomes significant because of non-negligible retardation effects. In this situation, consideration of higher order plasmon modes is indispensable to

#206576 - $15.00 USD Received 26 Feb 2014; revised 25 Apr 2014; accepted 29 Apr 2014; published 13 May 2014

correctly understand the optical and spectroscopic properties of the nanoparticles. Moreover, an understanding of the spatial features of plasmons based on fundamental modes of the system is useful to provide clear physical pictures of the phenomena.

Gold nanorods are an example of the importance of multipolar modes and retardation effects. In these almost one-dimensional particles, one can excite optically transverse and longitudinal plasmon modes which are polarized across and along the nanorod, respectively [13]. The transverse mode appears in a frequency region similar to that of the plasmon resonance of a small spherical nanoparticle. The resonance frequencies of longitudinal plasmon modes appear over a wide frequency range, and the mode with fewer nodes in its standing wave has the lower resonance frequency. The dipolar mode thus has the lowest resonance frequency, and all the resonances at higher frequencies are attributed to excitation of multipolar modes. The multipolar modes are not excited efficiently by conventional far-field irradiation when the particle size is small enough compared to the wavelength of the light, but they become significant when the particle size is large and the retardation effects are non-negligible. The spatial structures of these longitudinal modes have been visualized by near-field optical microscopy [13] or recently by electron-microscope based techniques [14–16].

In two-dimensional systems such as a circular gold nanoplate (nanodisc), the spatial structures of the plasmon modes are much more complicated. In addition, as the volume damping effect [17] becomes significant for these systems compared with nanorods, the spectral widths of individual modes are broad and consequently spectral overlaps between plasmon resonances are observed [18,19]. As a result, the optical properties of plasmons in nanodiscs are not as well understood as those of nanorods. To fully utilize the unique properties of plasmonic materials in practical applications, detailed knowledge of the plasmon modes is essential. In this study, we experimentally visualized plasmon modes of gold nanodiscs at various excitation wavelengths by scanning near-field optical microscopy. In contrast to nanorods, the observed images show complex features, and we find that theoretical simulation of the observed images is indispensable to rationally interpret the complex mode structures obtained. However, the plasmon modes of discs cannot be treated with any analytical approach. With numerical electromagnetic simulation approaches such as the finite difference time domain (FDTD) method [20] and the discrete dipole approximation (DDA) methods [21], the concept of modes cannot be introduced, although they can treat nanostructures of arbitrary shapes. We thus carried out assignments of the observed images based on the theoretical framework recently developed [22–26]. This approach enables us to give clear physical pictures of the spatial features of plasmon modes of metal nanoparticles observed in the experiments.

2. Experimental

Gold nanodiscs (diameter 400-800 nm, thickness 35 nm) were fabricated on a cover-slip by the electron-beam lithography/lift-off technique [27]. A home-made apertured scanning near-field optical microscope (SNOM) was operated under the ambient condition [28]. Aperture near-field fibre probes fabricated by chemical etching were purchased from JASCO Corp. The diameter of the aperture was determined to be 50-100 nm by using scanning electron micrographs and/or fluorescence images of single molecules. The sample substrate was mounted on the piezo-driven-stage for lateral scanning and the distance between the near-field aperture tip and the sample surface was regulated at 10-20 nm by a shear-force feedback mechanism. For near-field transmission measurements, either a Ti:sapphire laser or a Xe discharge lamp was used as a light source. Incident polarization was controlled by a combination of a half and a quarter wave plates. A gold nanodisc was locally illuminated through the aperture of the near-field probe, and the transmitted light through the sample was collected by an objective lens and detected by a polychromator equipped with a charge-coupled device (CCD). At each point in a whole scan area the intensity spectrum was

#206576 - $15.00 USD Received 26 Feb 2014; revised 25 Apr 2014; accepted 29 Apr 2014; published 13 May 2014

measured, and near-field extinction spectra were calculated as $-(I- I_0)/ I_0$, where I denotes the far field transmitted intensity taken with the sample present and I_0 the intensity from the bare substrate. Near-field transmission images were obtained by mapping the transmission $T = I/I_0$ at a given spectral range. The polarization of the transmitted light was characterized by a polarizer installed in front of the detector.

3. Results and discussion

Figure 1(a) shows a scanning electron micrograph (SEM) image of the fabricated gold nanodiscs. The dimensions of the nanodisc were 400 nm in diameter and 35 nm in height, as determined by SEM and topography measurements. Plasmon resonances of the disc depend on the aspect ratio (diameter / height) and shape of the disc, and the dipolar resonance for the disc with 400 nm diameter is expected to occur at wavelengths longer than 1000 nm [29]. Figure 1(b) shows a far field extinction spectrum of the disc. The dipolar resonance of the disc is far beyond the observed spectral range, and a shoulder and a broad band were observed at around 620 nm and near the infrared spectral region, respectively. These features are assigned to higher order plasmon resonances with the aid of theoretical calculations as discussed later. Figure 1(c) shows a polarized near-field extinction spectrum taken at the edge of the disc. The spectrum exhibits multiple peaks in the visible to near-infrared region similar to the far field spectrum. A sharp negative extinction peak at ~650 nm is typical of the near-field extinction measurements, and is attributed to the conversion of near-field radiation to propagating light [29,30]. The positive peaks at ~580 and ~780 nm are close to the shoulder and the band observed in the far field spectrum (Fig. 1b), and are attributed to plasmon resonances. We also found that the near-field transmission spectrum depends on the position of the probe with respect to the disc. For example, the negative peak is more pronounced at the center of the disc with respect to that observed at the edge. The position dependence of the near-field transmission spectrum implies that the spatial distribution of the oscillation amplitude of the mode excited at the longer wavelength is not uniform over the disc surface. Since the spatial characteristics of the mode are not directly apparent in the spectrum, which is a frequency-resolved data set, mode assignments of the plasmon resonances are not straightforward using only information from the spectrum. Near-field imaging enables spatial visualization of the mode and facilitates assignment of the mode by combining the data with theoretical simulations.

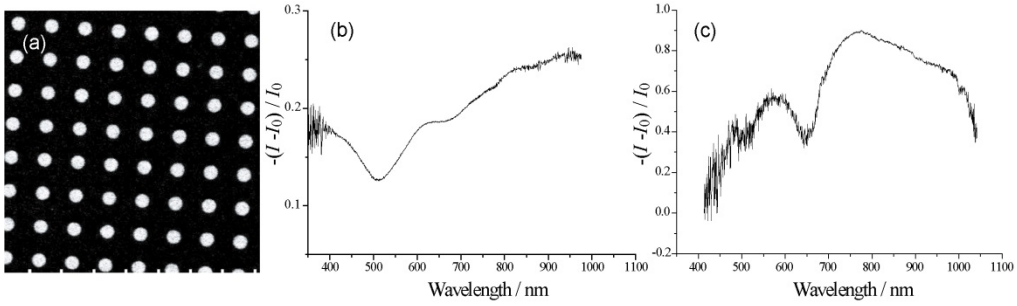

Fig. 1. (a) A SEM image of gold nanodiscs (diameter 400 nm × height 35 nm). (b) Far field transmission spectrum of the disc. (c) Near-field transmission spectrum taken at the edge of the disc.

Figures 2(a) and 2(b) show polarized near-field transmission images of the gold nanodiscs observed at 780 nm. The dotted circle indicates the approximate shape of the disc and the arrow shows the incident polarization direction. In the image, dark parts represent higher extinction (i.e. larger reduction of transmitted light due to scattering and absorption of incident light). Dark dots are roughly aligned perpendicularly to the polarization direction. The transmission image rotates 90 degrees as the polarization direction is rotated 90 degrees.

#206576 - $15.00 USD Received 26 Feb 2014; revised 25 Apr 2014; accepted 29 Apr 2014; published 13 May 2014

We reported previously, on the near-field excitation of a gold nanorod, that the extinction intensity of the longitudinal plasmon mode showed a $\cos^2\theta$ dependence upon the incident polarization direction, where θ is the angle between the long axis of the rod and the polarization direction [31]. This indicates that the excitation near-field is almost linearly polarized, and that there is no significant transfer of energy between orthogonal polarizations due to the interaction of the rod with the probe. The polarized optical near-field at an apertured probe tip utilized to visualize orientations of single-molecule transition moments with fluorescence excitation imaging [32] also indicates approximately linear polarization near the tip.

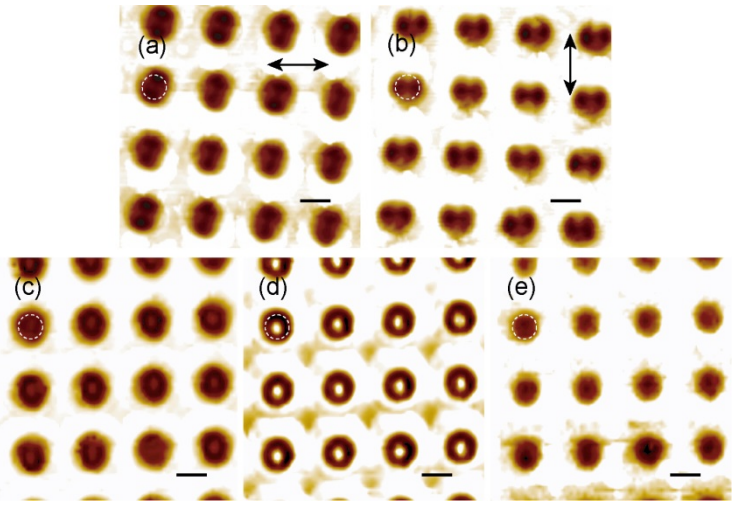

Fig. 2. (a,b) Polarized near-field transmission images of gold nanodiscs (diameter 400 nm × height 35 nm) observed at 780 nm. Arrows indicate the direction of incident polarization. (c-e) Unpolarized near-field transmission images for the gold nanodiscs. Observed wavelength: ~780 nm for (c), ~640 nm for (d), and ~520 nm for (e). Dotted circles indicate the approximate shape of the disc. Image size: 4 μm × 4 μm. Scale bar: 500 nm.

In addition to the polarized near-field transmission measurements described above, we performed near-field transmission measurements with unpolarized illumination and polarized light detection, and found that the near-field images show essentially the same spatial features and polarization dependences observed in Figs. 2(a) and 2(b). These observations support that the observed near-field images exhibit distributions of the polarized plasmon amplitudes excited by the incident light. An unpolarized near-field transmission image exhibits a doughnut-like spatial pattern as shown in Figs. 2(c) and 2(d). Spatial features of the near-field transmission image strongly depend on the observed wavelength. The transmission image observed at 520 nm in Fig. 2(e) shows a monotonous spatial feature, which is nearly identical to the topographic image (giving the geometrical shape) of the disc. The doughnut-like spatial feature with unpolarized light appears at wavelengths longer than ~580 nm. For discs smaller than 150 nm, the doughnut-like spatial feature was not observed at 800 nm. These observations show qualitative agreement with the electron energy loss spectroscopy (EELS) maps visualized by a high-resolution transmission electron microscope [33], while the polarization-dependent information is available only with the near-field measurements.

Spatial features of the images depend strongly on the size of the disc. Figures 3(a) and 3(b) show near-field transmission images of a larger gold disc (diameter 800 nm, thickness 35 nm) observed at 710 and 790 nm, respectively. The polarization direction of the detected light was vertical in the images. From the images, we found that fine spatial structures of excitation probability were observed, which varied depending on the wavelength of observation. For instance, the image observed at 710 nm exhibits a double-doughnuts-like feature, whereas that at 790 nm shows an extinction spot at the center combined with a single doughnut

#206576 - $15.00 USD Received 26 Feb 2014; revised 25 Apr 2014; accepted 29 Apr 2014; published 13 May 2014

feature. For the 400-nm diameter disc, the doughnut-like feature was observed only with unpolarized light detection, while for the 800-nm disc, the doughnut-like feature was observed with the polarized detection. Line profiles along the dotted lines through the centers of the discs in Figs. 3(a) and 3(b) are shown in Figs. 3(c) and 3(d), respectively. Transmission intensities oscillate along the lines. The period of the oscillation depends on the observed wavelength: the period increases as the wavelength increases. This finding qualitatively agrees with that for the spatial properties of longitudinal plasmon modes of gold nanorods. In the gold nanorod, the wave number of the longitudinal plasmon mode gets larger when its frequency gets higher, following the dispersion relation of the plasmon. Since the spatial feature observed in the near-field image of the disc is two-dimensional, it is not straightforward to interpret the feature based on the dispersion relation as in the one-dimensional case like nanorods. However, for the disc we also find a qualitative tendency for the spatial frequency of the image to increase with the frequency of the light for detection, which suggests that the two-dimensional waves of the disc plasmons follow a kind of dispersion relation between temporal and spatial frequencies.

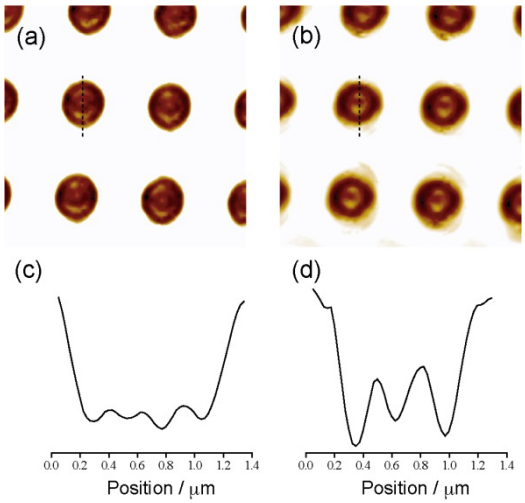

Fig. 3. (a,b) Near-field transmission images of gold nanodiscs (diameter 800 nm × height 35 nm). Observed wavelength: 710 nm for (a), 790 nm for (b). (c,d) Line profiles taken along the dotted lines in (a,b), respectively.

As we mentioned above, the near-field imaging provides valuable information on spatial features of plasmons, and is useful for assignments of the spectroscopic features of the metal nanoparticles to fundamental plasmonic modes. On the other hand, the spatial features of two-dimensional systems, such as the discs, are much more complex than those of one-dimensional rods, because of the higher degree of spatial freedom. The mode assignments for the discs are thus much more difficult than for rods. Consequently, to assign the plasmon resonances in the two-dimensional systems, a combination of imaging experiments and theoretical approaches is useful and in some cases essential. In the next section, we will analyze the near-field transmission images observed for the gold nanodics, based on a recently developed theoretical framework [22] where a set of fundamental electromagnetic modes are employed to expand the fields near the scattering object.

4. Theoretical analysis

In this section, we apply the theory of the principal modes of optical structures [22] to reproduce the spatial structures of experimental near-field transmission images of nanodiscs with diameters of 400 and 800 nm. In this theory, we find orthonormal sets of modes for the internal and scattered electromagnetic fields at the surface of the particles which are spatially correlated pairwise. The spatial correlations between pairs of internal and scattered modes can

#206576 - $15.00 USD Received 26 Feb 2014; revised 25 Apr 2014; accepted 29 Apr 2014; published 13 May 2014

be formulated in terms of "principal angles" and principal sine functions, sin ξ. This theory allows the identification of the physical mechanisms that determine the way in which these patterns evolve with the frequency of incident light and, correspondingly, the information that the experimental images provide. By applying this theory and using an approximate model of the experimental conditions, we reproduce all three kinds of images observed with polarized light (Figs. 2 and 3), as shown in Fig. 4, and explain the spatial structures and their transformation as the wavelength changes in terms of a relatively low number of optical modes. This approach allows us to analyze the spatial feature of the collective oscillation of conduction electrons that yields the near-field transmission image observed. A more detailed analysis of near field illumination will appear elsewhere. Briefly, the four fundamental components of the physical experiment that are included in the model are the SNOM aperture tip, the nanoparticle, the detector and the scattering medium (substrate). As in the experiments we consider the following two configurations. When the field sent through the SNOM tip is linearly polarized, the total intensity of the light is detected in the far field. When the field is unpolarized, the detector in the far field has a polarizer in front of it and collects only linearly polarized light. In the first case, the field radiated by the SNOM tip is represented by a coherent combination of one electric and one magnetic radiating point dipole, both located at the center of the planar aperture of the probe [34]. In the second case, the radiated field is represented by the incoherent superposition of two pairs of electric and magnetic dipoles at right angles. We use a dispersion relation for the gold material that includes both the bulk contribution and the effect of surface collisions [35]. The inclusion of collisions allows us to match accurately the pattern obtained at the experimental height of the tip above the particle.

Experiments have shown that the spatial structure of the observed near-field transmission image patterns are weakly dependent on the environment, although this may shift the range of wavelengths at which any given pattern is observed. For this reason, and for simplicity, we assume that the gold nanodiscs are immersed in the material of which the substrate is made, in this case borosilicate crown glass (BK7). However, the experiments could be more accurately modeled by considering the particle in a stratified medium [36]. We match the transmission image at the experimental resonance wavelength for the small disc of diameter 400 nm, Fig. 4(a) which corresponds to Fig. 2(b), and for the larger particle of diameter 800 nm at wavelength ca. 710 nm, Fig. 4(b) which corresponds to Fig. 3(a). We observe the longer wavelength near-field transmission pattern for the larger particle at wavelength blue-shifted with respect to the experiment by ca. 25 nm, Fig. 4(c) corresponding to Fig. 3(b). We simulate a detector with an effective numerical aperture of 0.85 (corresponding to a 60° cone in the far field). We have also simulated data for a variety of collection angles between 40 and 80 degrees. No significant change is found in the spatial structure of the simulated image, although the contrast between the bright and dark regions reduces slightly as the angle increases.

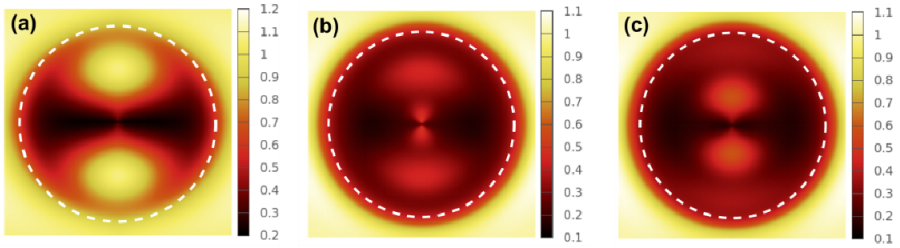

Fig. 4. (a) The theoretical near-field transmission image for the 400-nm diameter disc at an incident wavelength of 780 nm, corresponding to Fig. 2(b), calculated using an incident field linearly polarized along the vertical direction of the figure, where the colour scale corresponds to the unpolarized signal collected by the detector in the far field I normalized by the intensity of the incident field I_0. The corresponding images for the 800-nm diameter disc at (b) 705 nm and (c) 765 nm where the incident field is unpolarized and instead the signal collected by the detector is linearly polarized along the vertical direction of the figures.

#206576 - $15.00 USD Received 26 Feb 2014; revised 25 Apr 2014; accepted 29 Apr 2014; published 13 May 2014

The near-field transmission patterns can be understood in terms of groups of radiating modes which, due to the cylindrical symmetry of the discs, have an angular phase dependence $\exp(im\varphi)$, where φ is the azimuthal angle around the disc and m is the index of the component of the optical angular momentum along the symmetry axis. Therefore, we can group the modes according to their m index into separate scattering channels. Although there are an infinite number of possible optical angular momentum channels which may contribute to the surface field, only the channels with $m = 0, \pm 1, \pm 2$, and ± 3 contribute significantly to the observed transmission patterns, with the higher index channels having significantly less ability to transport energy into the far field. This is because the higher index m channels oscillate more rapidly around the disc and, due to the limited radial dimensions of these particles, the variations become much shorter than the wavelength of the incident light in the scattering medium, making it difficult for these channels to transport energy effectively. We in fact find that the $m = 0$ and ± 1 channels scatter the majority of the light and provide the basis of the near-field image patterns, with the higher index channels only adding fine structure. Within each channel, the incident field may excite many modes to an appreciable amplitude, which then combine to give the surface field. However, only a selection of these modes are capable of carrying energy [22], or information, into the far field and these are the modes that have the largest effect on the near-field transmission images. For the discs considered here, the light scattered by each channel can therefore be attributed to just a handful of modes.

For the figures, the direction of polarization is chosen to be along the vertical direction of the page. The images are normalized by the intensity of the incident field, I / I_0, where I is the intensity with the particle present and I_0 the intensity at the bare substrate without the particle. Near-field transmission images show the amount of light received at the detector due to the response of the particle to the near-field source. The effects of the particle on the amount of light transmitted towards the detector fall into 4 categories. Firstly, the disc can scatter light preferentially towards the detector, increasing the amount of light received. Alternatively, light may be scattered away from the detector, reducing the light received. The disc can also absorb light (again reducing the signal). Finally, for reasonably coherent sources of light, interference between the incident light and the light scattered by the disc may either increase or reduce the intensity in the far-field detecting aperture.

For the smaller particle (diameter 400 nm), the only significant contributions are from the $m = 0$ and ± 1 channels to the far field pattern, of which the $m = 0$ channel dominates the scattered light. To understand the properties of a scattering mode we consider the spatial correlation between this mode and the internal modes on the surface of the particle. Each principal scattering mode is spatially correlated with at most one principal internal mode, and this correlation is expressed as $\cos \xi$, which is the overlap integral of the tangent components of the pair of internal and scattering principal modes. $(\sin \xi)^{-1}$ represents the efficiency of this pair of modes to couple to an incident field with tangent components on the particle that are spatially correlated to the tangent components of the modes (even at resonance, when the efficiency is maximal, the mode pairs do not couple to incident fields with tangent components uncorrelated to those of the modes). Figure 5(a) shows the increase in efficiency of the dominant $m = 0$ mode as it approaches it's resonance at ~725 nm. Figure 5(b) shows

#206576 - $15.00 USD Received 26 Feb 2014; revised 25 Apr 2014; accepted 29 Apr 2014; published 13 May 2014

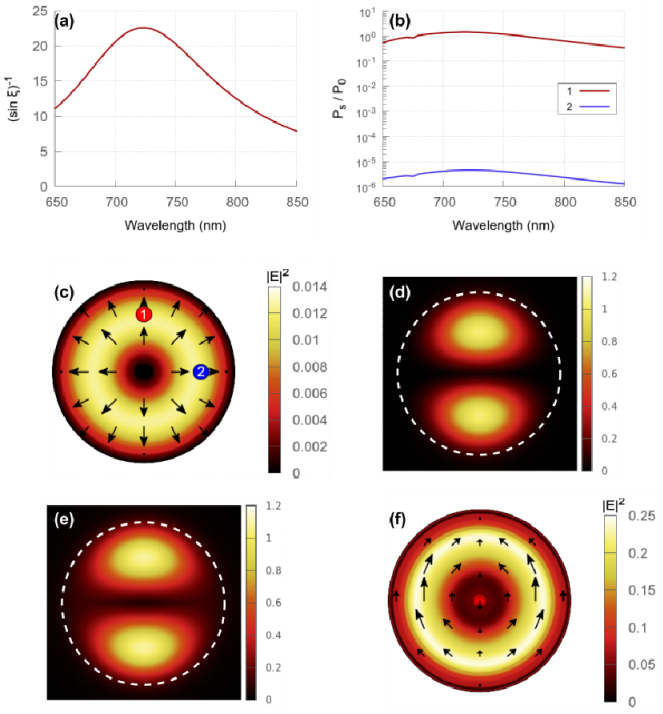

Fig. 5. (a) Plot of $(\sin \xi)^{-1}$ as a function of wavelength for the dominant $m = 0$ mode of the 400-nm diameter disc, where the cos ξ is the spatial correlation of internal and scattered surface fields of the mode. The plot shows the increase in excitability of the mode as it approaches its resonance at ~725 nm. (b) The amount of energy scattered towards the detector (P_s) for the two positions of the fibre tip marked in (c), normalized by the power of the incident field (P_0), as functions of wavelength. The feature at *ca.* 675 nm is due to two pairs of modes becoming almost degenerate and mixing properties. (c) The surface electric field intensity and polarization of the real part of the electric field for the dominant $m = 0$ mode. (d) Excitation map showing the contribution of the linearly polarized component of the dominant mode for the same channel. The scattered intensity, depicted by the color bar, is normalized to be in units of the incident field. (e) Excitation map, as in (d), but for all modes of the $m = 0$ channel. (f) As in (c) but for the superposition of the dominant modes of the $m = \pm 1$ channels.

the amount of energy scattered towards the detector for two positions of the fibre tip marked in Fig. 5(c) as a function of the wavelength. The ratio between the energy scattered for these two positions of the tip has a 20% variation for the range of wavelengths shown in Fig. 5(b). This is due to a change in the overlap between the mode and the input field caused by the dependence of the input field and of the mode on the wavelength. We note that for the disc considered here, contrary to what happens with spheres and infinite cylinders, the Maxwell's equations do not separate into a tangent and normal part, therefore there may be small variations in the tangent components of the modes at the surface of the disc as the wavelength is changed.

Figure 5(c) shows the surface electric field intensity and real part of the polarization for the dominant mode of the $m = 0$ channel, which is symmetrical about the axis of the particle. We expect that linearly polarized incident light will excite this mode in regions where the polarization of its surface electric field is closely aligned with the polarization of the incident field. This explains the two bright lobes shown in Fig. 5(d), where the electric fields are antiparallel. This mode accounts for over 85% of the light scattered by all of the modes in the $m = 0$ channel at 780 nm resulting in Fig. 5(d) almost exactly matching the scattered intensity

#206576 - $15.00 USD Received 26 Feb 2014; revised 25 Apr 2014; accepted 29 Apr 2014; published 13 May 2014

pattern of the entire $m = 0$ channel, shown in Fig. 5(e). This corresponds to the bright parts in the transmission pattern of Fig. 4(a), where I is nearly equal to I_0, i.e. the amount of scattered light received by the detector matches that without the disc present. The faint extra lobes evident horizontally in the outer parts of the transmission image of the $m = 0$ channel shown in Fig. 5(e) are due to a weakly excited secondary mode.

We can conclude that the bright parts of the image depicted in Fig. 4(a) are primarily due to a single mode of the disc. The two dark lobes in Fig. 4(a), aligned horizontally along the direction perpendicular to the polarization of excitation, can be attributed mainly to the destructive interference of the two dominant modes of the $m = \pm 1$ channels with the incident field. We find that the electric fields in these two dark lobes, towards the edges of the disc, are parallel as shown in Fig. 5(f). We also examined the origin of the negative peak around 650 nm observed in Fig. 1(c), by calculating the correlation between spatial modes exited in the near-field and the scattering channels transporting the radiation energy to the far-field. We found from the simulations that two modes of $m = \pm 1$ channels are responsible for scattered light at ~650 nm, and one of the modes predominantly yields forward scattering and makes a major contribution to the negative peak.

The near-field transmission images of the larger 800 nm diameter disc contain significant contributions from more than one m channel, each consisting of a greater number of modes than the smaller disc. The observed change of pattern with incident wavelength for the large disc, and indeed the relative contributions of the individual channels, can be explained in terms of modes moving on or off from resonance as the wavelength changes. When a radiating mode is close to resonance, it is excited with a greater amplitude and typically produces the majority of the observed far field intensity associated with that particular channel. Furthermore when a mode approaches the peak of its resonance it eclipses the contributions from the other modes, with up to 60% of the total energy radiated by that channel passing through the dominant mode in that case. For the 800 nm diameter disc at 705 nm, Fig. 4(b), we observe modes in both the $m = \pm 1$, shown in Fig. 6(a), and $m = \pm 3$ channels approaching resonance. As such these channels strongly influence the observed pattern at shorter wavelengths. For the pattern at 765 nm, Fig. 4(c), the $m = \pm 1$ and ± 3 modes have moved away from resonance and on the contrary, the modes of the $m = 0$ and ± 2 channels have moved towards resonance and therefore have more influence upon the observed accumulated pattern, highlighted in Fig. 6(a). Taking the $m = 0$ channel as an example, the dominant mode is near the peak of a resonance for the transmission image at 765 nm, Fig. 6(c), while its scattered intensity is four times weaker at 705 nm, Fig. 6(b). Scattering, combined with interference between some modes within both the $m = 0$ and $m = \pm 1$ channels determines the major features of the patterns, however there is also absorption present, particularly at the shorter wavelengths (primarily due to the $m = \pm = 1$ resonant modes). These effects are also present for the 400 nm diameter disc, but are small compared to scattering by the dominant $m = 0$ mode.

We remark that in our calculation we have assumed a perfect axial symmetry; as a consequence, only the $m = \pm 1$ and (assuming some small polarization in the z direction) the $m = 0$ channels can be excited by the incident field when the tip is on the symmetry axis (i.e., z-axis). This is the origin of the bright spots at the very center of Figs. 4(a)–4(c); breaking the axial symmetry would modify the center of these images. As a result we would expect this region of the pattern to show the largest discrepancy between experiment and theory.

The agreement of this analysis with the experiments demonstrates the advantage of the theoretical framework described here over numerical methods such as FDTD or DDA in identifying the plasmon modes responsible for near-field transmission images.

#206576 - $15.00 USD Received 26 Feb 2014; revised 25 Apr 2014; accepted 29 Apr 2014; published 13 May 2014

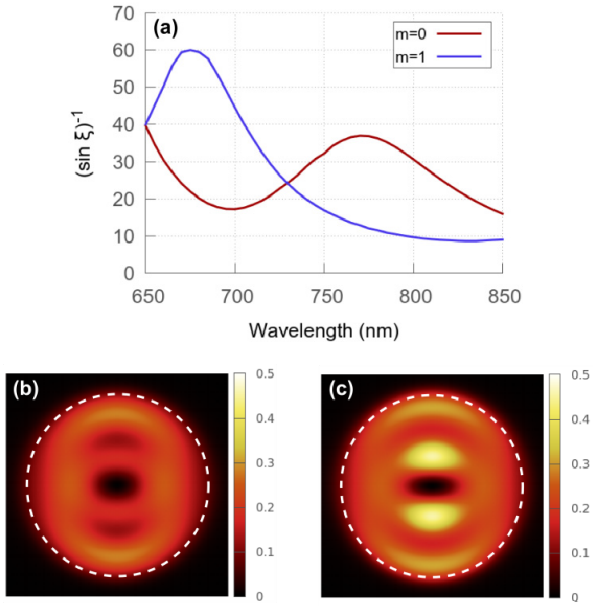

Fig. 6. (a) Plots of $(\sin \zeta)^{-1}$ as functions of wavelength for the dominant modes of the $m = 0$ and $m = 1$ channels for the 800-nm diameter disc are shown where the axes are the same as Fig. 5(a). (b,c) The normalized scattered intensity for the $m = 0$ channel far from resonance at 705 nm, (b), and close to it at 765 nm, (c).

4. Conclusion

We studied localized plasmons in single gold nanodiscs by near-field spectroscopic imaging measurements, and we found theoretically the plasmon modes that give rise to the spatial features of the experimental near-field transmission images. The observed near-field transmission images of the discs have characteristic spatial features that depend on the dimensions of the discs and the wavelength of observation, and can be quite complex. In contrast to one-dimensional systems like nanorods, it is not straightforward to assign fundamental plasmonic modes to the near-field images of two-dimensional discs. We achieved it by comparing the experimental images with the results of calculations based on a recently developed theoretical framework. We found that the simulated results reproduced the observed spatial features, and successfully assigned the observed images to fundamental modes of the systems. The theoretical method presently adopted enables us to interpret optical images of the systems based on the concept of fundamental electromagnetic oscillation modes. This approach is advantageous because it gives a clear physical explanation of the experimental transmission images of non-spherical metal nanoparticles. To extend the applicability of this approach, it is essential to generalize the numerical implementation of the theory to various particle shapes in a practical manner, which is in principle possible and now under way.

Acknowledgments

This work was supported in part by PRESTO program from Japan Science and Technology Agency, Grants-in-Aid for Scientific Research (Grant Nos. 19049001, 19049015, 22225002, 23225006, 24655020, 24350014, and 25109713) from the Japan Society for the Promotion of Science (JSPS) and from the Ministry of Education, Culture, Sports, Science and Technology, Nanotechnology Platform (Hokkaido University), the Royal Society (IE110759), and EPSRC (EP/K503174/1 and EP/K004670/1: Global - Promoting Research Partnerships: Strathclyde Escalator for Global Engagements in Research). This project was also supported by the JSPS and the Royal Society under the Japan – United Kingdom Research Cooperative Program.